Renewable Energy 197 (2022) 486–499

Contents lists available at ScienceDirect

Renewable Energy

journal homepage: www.elsevier.com/locate/renene

Economic configuration optimization of onboard annual thermoelectric generators under multiple operating conditions

WenChao Zhu [a,b], Wenlong Yang [a], Yang Yang [a,**], Yang Li [a], Hao Li [a], Ying Shi [a], Yonggao Yan [c], Changjun Xie [a,b,*]

[a] School of Automation, Wuhan University of Technology, Wuhan, 430070, China
[b] Hubei Key Laboratory of Advanced Technology for Automotive Components, Wuhan University of Technology, Wuhan, 430070, China
[c] State Key Laboratory of Advanced Technology for Materials Synthesis and Processing, Wuhan University of Technology, Wuhan, 430070, China

ARTICLE INFO

Keywords:
Exhaust gas fluctuation
Annular thermoelectric generator
Multi-objective optimization
Economy performance optimization

ABSTRACT

Highly variable automobile operating conditions and the ever-fluctuating exhaust parameters pose fundamental challenges to optimizing the design of automobile annular thermoelectric generators (ATEGs). This paper establishes an advanced non-isothermal mathematical model of ATEGs using the finite element method for solving this problem. First, the effects of different vehicle operating conditions on the optimal thermoelectric semiconductor volume are investigated. Based on the results, the optimal range for selecting the thermocouple volume is determined. Aiming to maintain a high net power of ATEG under variable operating conditions, two new schemes are proposed to optimize the system configuration, including 1) a weighted power deviation method and 2) a multi-objective intelligent optimization algorithm. Then, a new method for assessing the power generation cost is proposed for the ATEG. Combined with the characteristics of vehicle exhaust fluctuation in the New European Driving Cycle, the economics of the above two schemes are calculated and compared, and the optimal design is obtained. The results show that the optimal ATEG system configuration is: the PN couple volume in a single ring is 5.0625×10^{-6} m^3, the total PN couple volume is 2.835×10^{-4} m^3, and the net power and the efficiency can reach 20.85 W and 3.9%, respectively. The proposed model and method contribute to optimize the structural configuration of the on-board ATEGs, and can be further extended for other application scenarios of the thermoelectric generator system.

1. Introduction

1.1. Literature review

Renewable and clean energy conversion technologies have attracted extensive research interests due to the ever-increasing carbon emissions and depletion of fossil fuels in the last two decades. As an important branch, there has been active research on thermoelectric generators (TEGs) due to their high reliability and long life. Unfortunately, due to their low energy conversion efficiency, the applications of TEGs are limited, most in the fields such as aerospace [1,2], wearable devices, and vehicle-mounted TEGs [3–5].

For a traditional diesel locomotive, at least one-third of the energy is consumed and emitted in the form of waste heat, and the potential to use TEGs to recover the thermal energy in this application is promising. Fig. 1 shows a schematic of a practical application of an automotive TEG [6].Fig. 1(a) shows a schematic and underneath view of the location of the automotive TEG in an SUV. Generally, automotive TEGs are installed after the exhaust catalytic converter, close to the engine and with a certain degree of freedom of installation. Fig. 1(b) shows the exploded view of the TEG. The 1 to 7 in the figure are: cover, cooling water tank, thermoelectric modules, heat exchanger, butterfly valve, exhaust inlet/outlet, and junction, respectively.

Vehicle-mounted TEGs typically consist of many thermoelectric modules (TEMs) in electric series and thermal parallel. A TEM typically consists of several p/n-type semiconductor legs. Factors such as the temperature difference between the two sides of the legs, the thermoelectric material, and the geometry affect the energy conversion efficiency and output power of the TEM [7]. In the automobile exhaust gas recovery process, since the temperatures of the exhaust gas and the ambient air are limited in specific ranges, the operating temperature and

** Corresponding author. .
* Corresponding author. School of Automation, Wuhan University of Technology, Wuhan, 430070, China. .
E-mail addresses: whutyangyang@whut.edu.cn (Y. Yang), jackxie@whut.edu.cn (C. Xie).

https://doi.org/10.1016/j.renene.2022.07.124
Received 21 March 2022; Received in revised form 12 July 2022; Accepted 25 July 2022
Available online 7 August 2022

Nomenclature

symbols

a	length of ATEG, m
C	weighted percentage, %
D	hydraulic diameter, m
dev	percentage deviation, %
dev_m	weighted power deviation value of m_f
$dev_{m.T}$	weighted power deviation value of m_f and T_{fin}
f_z	pressure drop, Pa
h	heat transfer coefficient, $W{\cdot}m^{-2}\ K^{-1}$
I	current, A
H	height of p- or n-type leg, m
W	thickness of p or n-type leg, m
L	inner arc length of p or n-type leg, m
m	mass flow rate, $g{\cdot}s^{-1}$
n	number of thermocouples
P	power, W
Q	quantity of heat, W
K	thermal conductance, $W{\cdot}K^{-1}$
R	radius, m/resistance, Ω
T	temperature, K
V	volume, m^3
v	flow velocity, $m{\cdot}s^{-1}$
Re	Reynolds number
S	heat transfer area, m^2
F	Darcy resistance coefficient
c_p	specific heat capacity, $J{\cdot}g^{-1}\ K^{-1}$

Superscript

i	unit i
j	unit j

Subscript

a	cold air fluid
ain	inlet cold air fluid
aav	averaged value of cold air fluid in a unit
f	hot fluid
fin	hot fluid of inlet
fav	averaged value of hot fluid in a unit
p	P-type leg
n	N-type leg
L	external load
opt	optimal value
net	net value
$pump$	consumed pump value
x	x direction
r	r direction
h	hot end
c	cold end
vsp	volumetric specific power
pn	PN couple

Abbreviations

FTEG	flat thermoelectric generator
ATEG	annular thermoelectric generator
TEM	thermoelectric module
ATEM	annular thermoelectric module

Greek symbols

α	Seebeck coefficient, $V{\cdot}K^{-1}$
λ	thermal conductivity, $W{\cdot}m^{-1}\ K^{-1}$
ρ	electrical resistivity, Ω·m
δ	angle, rad
μ	dynamic viscosity coefficient, Pa·s
η	efficiency, %

the materials of the TEMs are relatively fixed. A conventional onboard TEG composed of many cuboid-shaped legs is called FTEG. Liu et al. [8] designed an exhaust pipe heat exchanger for an FTEG and carried out a road test for validation. Shu et al. [9] investigated segmented leg FTEG to match the large radial temperature gradient. The FTEG is installed in the low-temperature region of the vehicle's exhaust pipe to increase the TEG conversion efficiency. Liu et al. [10] studied the thermoelectric conversion performance of the variable cross-section semiconductor legs under eight different boundary conditions. The results showed that the variable cross-section PN legs have higher conversion efficiency than the rectangular parallelepiped leg under normal conditions. Although the structure of the PN leg in TEGs has been studied and improved through the years, the flat-type PN legs are still used in existing commercial TEGs. These flat-type PN legs cannot fully fit the circular exhaust pipe commonly used in automobiles, causing high contact resistance and excessive energy loss [11,12].

In this regard, Shen et al. [13] proposed a novel annular thermoelectric generator (ATEG). The authors analyzed the effects of the PN couples geometric characteristics on thermoelectric conversion characteristics under different parameters of the heat source and external loads theoretically. On this basis, Kaushik et al. [14] considered the Thomson effect to derive new expressions for optimal current under maximum output power, exergy, and efficiency conditions. Later, the authors applied the ATEGs to solar heating tubes. The results showed that the ATEG outperforms the FTEG in thermoelectric conversion performance [15]. The effects of external load, heat flow density, cold end heat transfer capacity, and tube leg height on the heat transfer performance were analyzed by Shen et al. [16]. The ATEG performance was also compared with that under constant temperature conditions. In our previous investigation, four different boundary conditions were applied in three typical application scenarios to study the effects of geometric structure on thermoelectric performance [17]. Subsequently, Weng et al. [18] proposed an ATEG with variable angle PN legs, which increased the output performance by 35%.

This new structure of ATEG needs to be systematically analyzed at the TEM level for practical applications since existing works focus on simplified and stable operating conditions. For example, it was shown that the TEM parameters can be changed for the constant heat flux condition to maximize the energy conversion efficiency and output power [19]. However, for onboard TEGs, the velocity, temperature, density, and mass flow rate of exhaust gas from the engine changes with the working conditions. TEMs are arranged on the outside of the exhaust pipe along the engine exhaust direction, and the actual working points change significantly with the temperature gradient [20]. From the perspective of TEG system integration, it is not advisable to use too many TEMs in a TEG since the total resistance increases linearly to the module length if all modules are connected in series. In addition, when considering temperature gradients, the electromotive force generated by each PN couple decreases with the reduction of the temperature difference between the two sides, which conforms to the Seebeck effect [21]. In addition, the length of the exhaust pipe has to be increased in order to install more TEMs, which could cause the rising exhaust back pressure of the automobile engine, resulting in a decrease in the overall net power [22]. Aiming to solve this problem, Yang et al. [23] designed an ATEG with a concentric annular heat exchanger, which can increase the total output power of the TEG while avoiding excessive back pressure. Another practical situation is that the engine exhaust parameters vary significantly with the operating conditions. As will be exhibited in

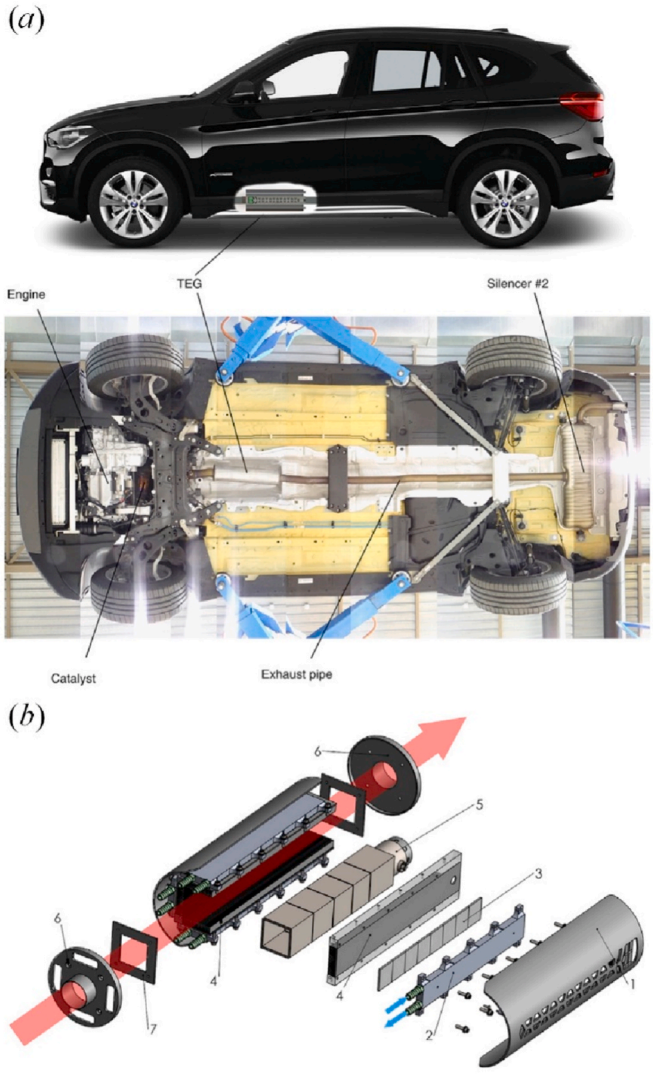

Fig. 1. Schematic diagram of the (a) practical application of automotive TEG and (b) exploded view of the TEG prototype [6].

this paper, taking this feature into designing and optimizing the onboard thermoelectric generator is beneficial but rarely noticed in the literature.

1.2. Research gaps and paper contributions

Several previous publications have investigated various optimization methods for TEG [24,25,26]. However, the results of the FTEG optimization may not be directly applicable to ATEGs. In addition, the optimizations of ATEG are primarily based on a single thermocouple, and the results can be significantly different when applied to the whole ATEG. This is particularly concerned for ATEG applications for automotive waste heat recovery, where some new features exist. Most researchers conducted their studies under specific exhaust parameters. Based on the characteristics of TEG models, none of the existing studies considered that the engine exhaust parameters can change with the operating conditions of the automobile. Therefore, in view of the coupling relationship between the parameters of ATEG systems and the influence of the variable parameter heat source, a practical design approach for onboard ATEGs to increase the overall net power and economic efficiency remains to be researched under various working conditions.

In this connection, we developed an integrated numerical model of ATEGs, with which the optimal thermoelectric performance is studied. The volume-specific power is defined, and it is used to compare the thermoelectric performances of FTEGs and ATEGs. A weighted power deviation analysis method is proposed for the first time to optimize the ATEG design used in engine waste heat recovery under variable operating conditions. This method comprehensively considers the fluctuation of heat source parameters so that the ATEG system maintains high net power output during operation. Subsequently, the thermoelectric semiconductor volume configuration of ATEG is optimized using the non-dominated sorting genetic algorithms-II (NSGA-II). Finally, by comparing the economics of the two methods, the optimal solution was determined. In this regard, the innovations and main contributions of this paper are:

1) The volumetric specific power of thermoelectric semiconductors is introduced. The thermoelectric performances of FTEG and ATEG are compared with the same thermoelectric semiconductor volume and under different working conditions.
2) The influence of different heat source parameters on the thermoelectric performance of ATEG is analyzed. The range of optimal design of the thermoelectric semiconductor volume is obtained.
3) Combined with the changes in the exhaust parameters of the New European Driving Cycle (NEDC), the weighted power deviation method and NSGA-II multi-objective optimization method are proposed to optimize the economy of ATEG. As a result, the optimal system configuration is obtained.

1.3. Paper organization

The layout of the article is as follows: The TEG numerical model is introduced and developed in Section 2. Then, the theoretical and experimental verification of the model is provided in Section 3. The thermoelectric performance analysis of ATEG and system economic performance optimization methods are next introduced in Section 4. Finally, Section 5 gives the main concluding remarks.

2. ATEG system modeling

2.1. System configuration and description

Fig. 2(a) shows a 3D schematic diagram of the ATEG module. The ATEG module consists of n_x ring-like thermoelectric units, indexed by $i = 1, 2, \ldots, n_x$. Each thermoelectric unit consists of n_r thermocouples, indicated by $j = 1, 2, \ldots, n_r$. All the thermocouples are connected in series and distributed evenly. We denote each thermocouple as a PN couple or a PN calculation unit. The engine exhaust gas is considered to flow into the annular module pipe in the axial direction. The heat in the exhaust gas is transferred to the ambient through the hot end (inner) and the cold end (outer) of the thermocouples in the radial direction. As shown in Fig. 2(b), the radius of the ATEG is R. H, W, and L denote the height, thickness, and the inner arc length of p- or n-type legs, respectively. Furthermore, the inner arc length corresponds to an angle δ.

Fig. 3 shows how temperature changes in a PN calculation unit. $Ti,j\ f$ and $Ti + 1,j\ f$ denote the temperatures of the exhaust gas (hot fluid) flowing into and out of the PN calculation unit, respectively. Similarly, $Ti,j\ a$ and $Ti + 1,j\ a$ represent the temperatures of the air (cold fluid) flowing into and out of the calculation unit, respectively. The inlet temperatures of the hot fluid and the cold fluid of the first thermoelectric unit are denoted as T_{fin} and T_{ain}, respectively. $Ti,j\ h$ and $Ti,j\ c$ are the temperatures at the hot and cold ends of the PN couple, respectively. Furthermore, for later use, we define the average temperatures as the average of the fluid temperatures that enter and leave the calculation unit, i.e.,

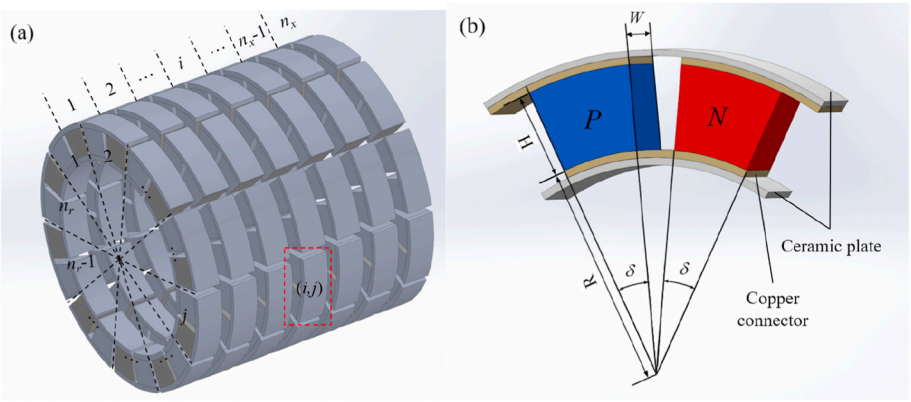

Fig. 2. 3D schematic diagram of (a) an ATEG module and (b) a PN couple.

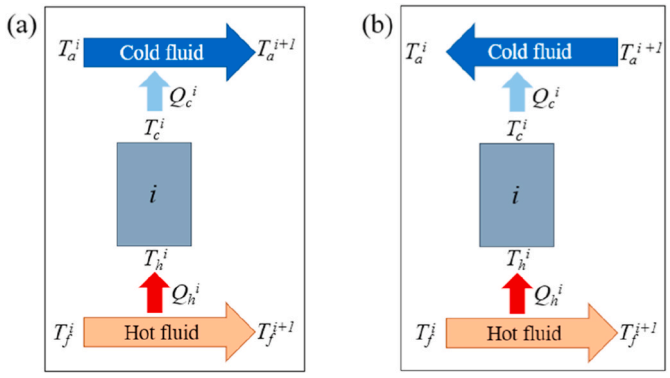

Fig. 3. Structural and temperature distribution diagram of ATEGs. (a) Coflow; (b) Counterflow.

$$\begin{cases} T_{fav}^{i,j} = \left(T_f^{i,j} + T_f^{i+1,j}\right)/2 \\ T_{aav}^{i,j} = \left(T_a^{i,j} + T_a^{i+1,j}\right)/2 \end{cases} \tag{1}$$

Fig. 3 also shows two typical cooling methods. The relationship between the two fluids can be regarded as the coflow (CO) if the flow directions are the same, as shown in Fig. 3(a). In contrast, the relationship in Fig. 3(b) is called counterflow (COU) if the directions are opposite.

2.2. Basic assumptions and model parameters

In order to establish a mathematical model based on the configuration shown in Fig. 1, the following assumptions are made [20].

1) The contact resistance of copper sheet and solder, contact thermal resistance, and ceramic sheet are not considered;
2) The Thomson effect is not considered since it is usually extremely weak;
3) Commonly used commercial Bi_2Te_3 thermoelectric material is used, and the thermoelectric properties do not change with temperature;
4) The air convection and heat radiation are neglected, for both that between hot and cold ends and that between the thermocouple arms.

Basic parameters of Bi_2Te_3 thermoelectric material are shown in Table 1 [20].

According to Ref. [27], the temperature T_{fin} of the heat source used for heat recovery is between 250 °C and 600 °C, and the mass flow rate m_f vary between 10 g s^{-1} and 50 g s^{-1}. Here, we adopt the most commonly used values: $T_{fin} = 400$ °C and $m_f = 20$ g/s. All parameters of the hot and cold fluids are given in Table 2 [28,29].

Table 1
Basic parameters of p- and n-type semiconductors.

Description	p-type semiconductor	n-type semiconductor
Dimensions of PN couple (height/width/ inner circular arc length) H/W/L	5/5/5 mm	5/5/5 mm
Seebeck coefficient	2.037×10^{-4} V K^{-1}	-1.721×10^{-4} V K^{-1}
Thermal conductivity	1.265 W m^{-1} K^{-1}	1.011 W m^{-1} K^{-1}
Resistivity	1.314×10^{-5} Ω m	1.119×10^{-5} Ω m

Table 2
Parameters of hot and cold fluids.

Description	Hot fluid	Cold fluid
Inlet temperature	400 °C	30 °C
Mass flow rate	20 g s^{-1}	10 g s^{-1}
Specific heat capacity	1.12 J g^{-1} K^{-1}	1.0 J g^{-1} K^{-1}
Heat transfer coefficient	80 W m^{-2} K^{-1}	80 W m^{-2} K^{-1}

2.3. Model development

The heat transfer process in ATEGs can be described by three sets of internal heat transfer equations. First, by considering the Peltier effect, Fourier effect, and Joule's law, we have

$$\begin{cases} Q_h^{i,j} = \alpha_{pn} I T_h^{i,j} + K_{pn}\left(T_h^{i,j} - T_c^{i,j}\right) - 0.5 I^2 R_{pn} \\ Q_c^{i,j} = \alpha_{pn} I T_c^{i,j} + K_{pn}\left(T_h^{i,j} - T_c^{i,j}\right) + 0.5 I^2 R_{pn} \end{cases} \tag{2}$$

where the subscripts "h" and "c" indicate the hot end and the cold end, respectively, I is the generated current, and the Seebeck coefficient α_{pn}, thermal conductance K_{pn}, and resistance R_{pn} are determined by

$$\alpha_{pn} = \alpha_p - \alpha_n \tag{3}$$

$$K_{pn} = \frac{\delta W\left(\lambda_p + \lambda_n\right)}{\ln(R+H) - \ln(R)} \tag{4}$$

$$R_{pn} = [\ln(R+H) - \ln(R)]\frac{\rho_p + \rho_n}{\delta W} \tag{5}$$

where λ and ρ are the thermal conductivity and resistivity, respectively. The subscripts "p" and "n" indicate p- and n-type semiconductor legs, respectively.

Second, the temperature difference between the surface of the thermocouple and the fluid can be expressed by the Newton's law of heat transfer, i.e.,

$$\begin{cases} Q_h^{i,j} = h_f \ \ S_h\left(T_{fav}^{i,j} - T_h^{i,j}\right) \\ Q_c^{i,j} = h_a \ \ S_c\left(T_c^{i,j} - T_{aav}^{i,j}\right) \end{cases} \tag{6}$$

where h represents the heat transfer coefficients. The subscripts "f" and "a" indicate the heat transferred from hot fluid to the surface of the thermocouple and the heat transferred from the surface of the thermocouple to air, respectively.

Third, the heat transfer rates between the hot and cold fluid and the TEM are

$$\begin{cases} Q_h^{i,j} = c_{pf} m_f \left(T_f^{i+1,j} - T_f^{i,j}\right)/n_r \\ Q_c^{i,j} = c_{pa} m_c \left(T_a^{i+1,j} - T_a^{i,j}\right)/n_r \end{cases} \tag{7}$$

where m denotes the mass flow rate. c_{pf} and c_{pa} represent the specific heat capacities for the hot and cold fluid, respectively.

The current I and output power P_{ATEG} of ATEGs are evaluated by

$$I = \sum_{i=1}^{n_x} \sum_{j=1}^{n_r} \alpha_{pn} \left(T_h^{i,j} - T_c^{i,j}\right) / \left(R_L + R_{pn} n_x n_r\right) \tag{8}$$

$$P_{\mathrm{ATEG}} = \sum_{i=1}^{n_x} \sum_{j=1}^{n_r} \left(Q_h^{i,j} - Q_c^{i,j}\right) \tag{9}$$

The pump can cause power loss to drive hot fluid through the exhaust pipe. The pumping power is determined by [26].

$$P_{\mathrm{pump}} = f_z \left(m_f / \rho_f\right) \tag{10}$$

$$f_z = 4f(a/D)\left(v_f^2 \rho_f / 2\right) \tag{11}$$

$$v_f = m_f / \left(A \rho_f\right) \tag{12}$$

where ρ_f represents the density of the hot fluid, f_z denotes the pressure drop of exhaust gas, a is the length of the ATEG in the x-direction, v_f is the average axial velocity of hot fluid, and A represents the axial sectional area of the pipe through which the fluid flows. D denotes the hydraulic diameter, assuming $D = 2R$ in this work. In addition, f in (13) is the Darcy resistance coefficient determined by Ref. [30]:

$$\begin{cases} f = \dfrac{0.0791}{\mathrm{Re}_f^{0.25}}, 2000 < \mathrm{Re}f \le 59.7 / \left(\dfrac{2Hr}{D}\right)^{\frac{8}{7}} \\ \dfrac{0.5}{\sqrt{f}} = -1.8\lg\left\{\dfrac{6.8}{\mathrm{Re}f} + \left(\dfrac{Hr}{3.7D}\right)^{1.11}\right\}, 59.7 / \left(\dfrac{2Hr}{D}\right)^{\frac{8}{7}} < \mathrm{Re}f \le 665 - 765\lg\left(\dfrac{2Hr}{D}\right) / \left(\dfrac{2Hr}{D}\right) \\ f = 0.25 / \left\{2\lg\left[3.7D / \left(\dfrac{2Hr}{D}\right)\right]\right\}^2, \mathrm{Re}f > 665 - 765\lg\left(\dfrac{2Hr}{D}\right) / \left(\dfrac{2Hr}{D}\right) \end{cases} \tag{13}$$

where H_r denotes the internal surface roughness of the heat exchanger with $H_r = 5 \times 10^{-6}$ m, μ_f denotes the dynamic viscosity coefficient of the exhaust gas, and the Reynolds number Re_f is calculated by

$$\mathrm{Re}_f = D v_f \rho_f / \mu_f \tag{14}$$

The net power and the efficiency of the ATEG are calculated by

$$P_{\mathrm{net}} = P_{\mathrm{ATEG}} - P_{\mathrm{pump}} \tag{15}$$

$$\eta = P_{\mathrm{net}} / \sum_{i=1}^{n_x} \sum_{j=1}^{n_r} Q_h^{i,j} \tag{16}$$

The performance of the ATEG is analyzed based on the total volume of PN couples V_x, determined by the number of thermocouples n_x, i.e.,

$$V_x = 2W\left[\delta(R+H)^2 / 2 - LR/2\right] n_r n_x \tag{17}$$

Note that n_x is also used to represent the length of ATEG in this work.

2.4. Model solution method

It can be clearly seen that there is a nonlinear coupling effect between the electrical and thermal quantities of the ATEG. Specifically, the current I affects the internal temperature distribution of ATEG, and the temperature distribution also determines the current and voltage of the module. Therefore, we propose an iterative numerical method to solve the nonlinear model, and the flowchart is presented in Fig. 4.

3. Model validation

In this section, the comprehensive ATEG model established in the previous section will be compared and validated. First, the simulated results are compared with the net power in Ref. [31] under the same model parameters. In Ref. [31], the authors compared four different methods as well as the effects of heat transmission enhancement based on ATEG. Fig. 5(a) shows the net power of ATEG with different exhaust mass flow rates. The maximum error between the reference data and the model in this paper is 1.5%. This slight difference is due to the simplification of the current calculation method.

Next, the model was verified by comparing the results with the experimental data based on an FTEG. Since the PN couples of the annular thermoelectric module (ATEM) can be regarded as a flat plate when the radius of the ATEM is long enough, we used the same parameters provided in Ref. [29]. A schematic diagram of the TEG experimental setup established by Niu et al. is shown in Fig. 6. The system consists of a heat exchanger/thermoelectric converter, a cold fluid loop, a thermal fluid loop, and a data acquisition system. A commercial Bi_2Te_3-based thermoelectric module, measuring 40 mm × 40 mm × 4.2 mm, is used, consisting of 127 thermocouples with a maximum temperature difference of 68 K.

The comparison of ATEG power under different loads is shown in Fig. 5(b). A maximum error of 8% exists between the proposed model and the experimental data. This is mainly due to the difference in the thermoelectric characteristics between the developed model and the experiment results. In this model, the thermoelectric characteristics of the thermocouples are considered constant. In the experiment, the thermoelectric characteristics are temperature-dependent. It shows that the proposed mathematical model can accurately predict the ATEG output power since it can be used to generate the data close to the experimental results.

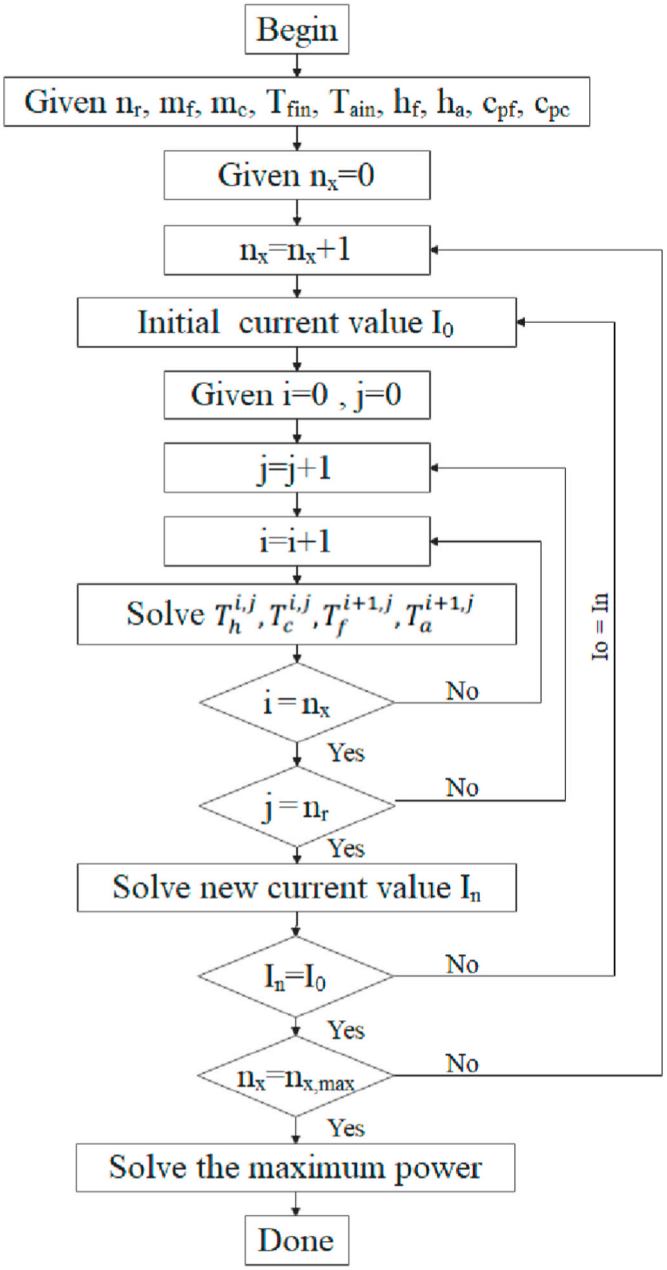

Fig. 4. Flowchart of the model solution procedure.

4. Results and discussion

4.1. Analysis of ATEG thermoelectric conversion performance

In this subsection, some thermoelectric characteristics of ATEG are presented, and the temperature gradient characteristics of the numerical model are analyzed. In addition, the thermoelectric characteristics of FTEG and ATEG are compared.

4.1.1. Basic characteristics of ATEG

Fig. 7 presents the voltage U and current I for the module length n_x at $n_r = 19$, which is determined by the inner radius of the annular channel ($R = 38$ mm) in practical applications. The simulation results shows that as n_x increases, the voltage increases rapidly at first, and then the rate of change slows down. As the total semiconductor volume increases, the current decreases.

Fig. 8 shows the variations net power and maximum power of the

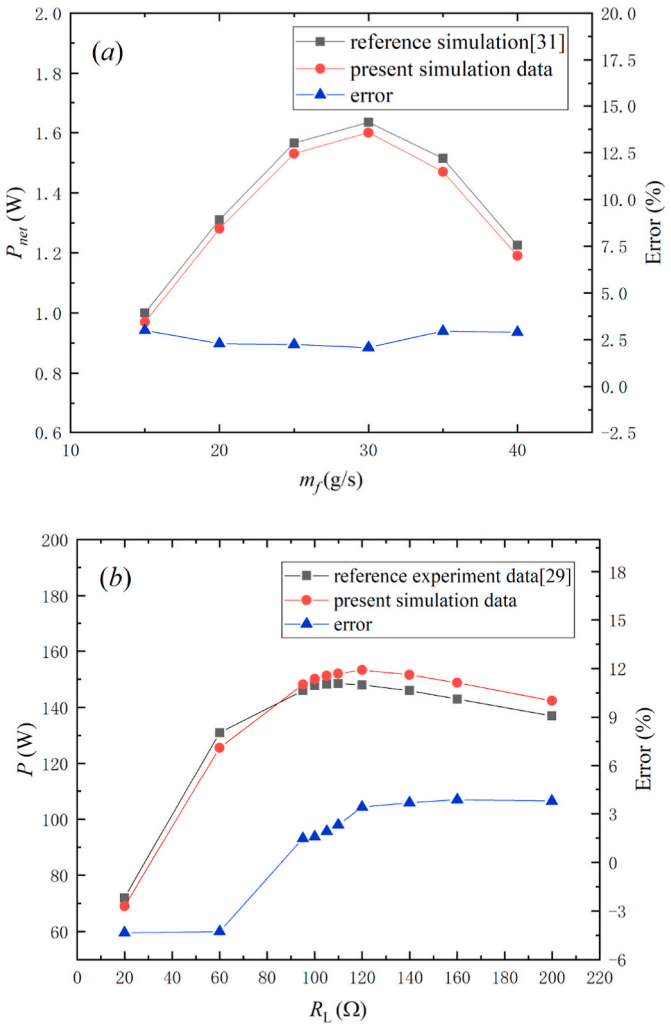

Fig. 5. Model validation. (a) Compared with simulation data; (b) Compared with experimental data.

proposed ATEG model with V_x in these two cases. $P_{\text{ATEG-CO}}$, $P_{\text{ATEG-COU}}$, $P_{\text{net-CO}}$, and $P_{\text{net-COU}}$ reach the peak value at a certain length, respectively. The peak power and net power of an ATEG in COU situation are better than those in CO situation, which are higher than 14.6% and 16.8%, respectively. Although the performance of COU is better,

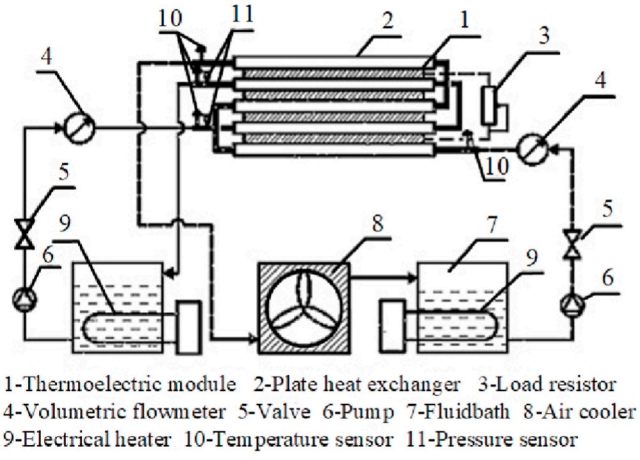

Fig. 6. The schematic diagram of an experimental setup of TEG [29].

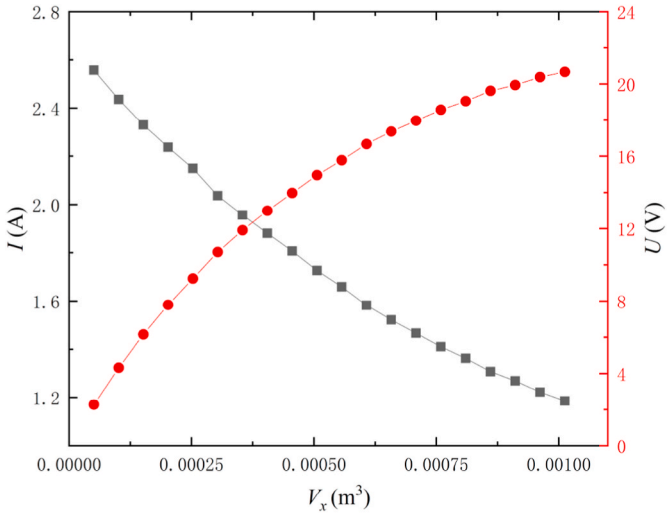

Fig. 7. Voltage and current versus V_x.

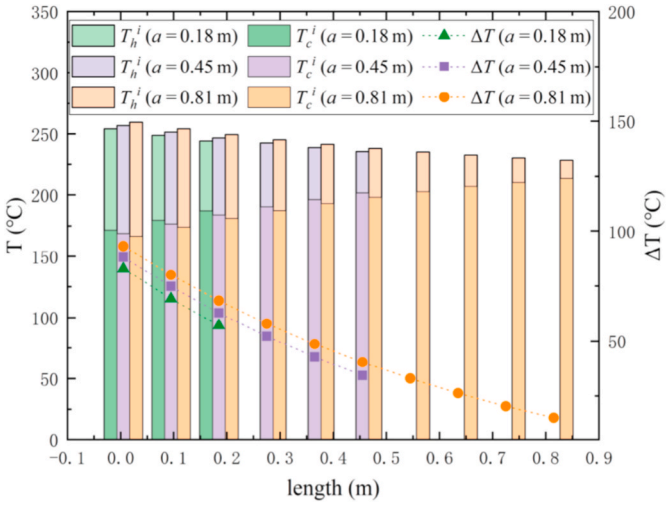

Fig. 9. Temperature distributions with different module lengths.

changing the layout of the exhaust system may involve adjustments to the entire vehicle and may increase exhaust backpressure. The direction of the exhaust pipe of the BMW 530i is roughly the same as the direction of airflow during driving. The remaining of this work is based on the CO situation.

When considering the power loss caused by the engine exhaust back pressure, the maximum value of the $P_{\text{net-CO}}$ is obtained at a shorter ATEG length than that of the $P_{\text{ATEG-CO}}$. This is because the longer the annular channel is, the greater the required pumping power should be needed. Therefore, an optimal thermoelectric semiconductor volume exists to maximize the $P_{\text{net-CO}}$ of ATEG, which will be elaborated later.

The characteristics of $P_{\text{ATEG-CO}}$ can be interpreted by the temperature difference of ATEG in the direction of fluid flow. In the case of different ATEG lengths, the temperature distribution at both ends of ATEG is shown in Fig. 9. When the radius of the ATEG is the same ($R = 38$ mm), the lengths of three different modules are studied:0.18 m, 0.45 m, and 0.81 m. The temperature difference decreases with the direction of fluid flow, which accounts for the variation of module voltage in Fig. 7. Because the thermal energy of the hot fluid is gradually transferred to the cold fluid, the operating temperature difference of the thermocouple decreases with the direction of fluid flow. In thermoelectric modules of different overall lengths, the temperature distribution is always similar at the same length from the heat flow inlet. The total resistance of a module is linearly related to the volume and number of thermocouples, resulting in a continuous decrease in current.

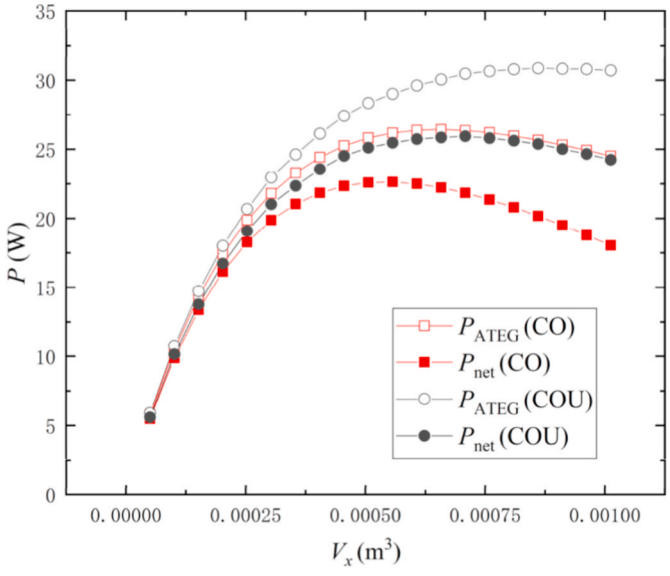

Fig. 8. Module power output and net power versus V_x.

4.1.2. *Comparison with FTEG*

For FTEG and ATEG with the same volume, the influence of different vehicle operating conditions on the output power characteristics of these two TEGs has not been reported in the literature. Therefore, this part analyzes and compares the output performances of FTEG and ATEG under different operating conditions.

To compare and analyze thermoelectric characteristics of FTEG and ATEG, a mathematical model of FTEG is also established, using the same calculation method. The boundary conditions, exhaust gas parameters, number of PN couples, and other conditions of the two models are also the same. The difference is that the PN couples are set to a regular shape, and the width, length, and height are all 5 mm [17]. Since the radius of the ATEG is $R = 38$ mm, to ensure the same module area, the width of the FTEG module is set to the circumference of the ATEG, which is 238.6 mm. Since the physical structures of the TEM are different both in terms of PN couples and the integrated structure, the volumetric specific power P_{vsp} is introduced here to facilitate the comparison of the thermoelectric performance, i.e.,

$$P\text{vsp} = P/V \tag{18}$$

Deviation of P_{vsp} between the ATEG and FTEG is denoted as ΔP_{vsp}

$$\Delta P\text{vsp} = P\text{vsp} - \text{ATEG} - P\text{vsp} - \text{FTEG} \tag{19}$$

Fig. 10(a) shows the change of P_{vsp} with the volume of PN couples at different m_f. It can be seen that the difference between the volumetric specific power of ATEG and FTEG increases as the mass flow rate increases, while the rate of change is relatively low. A larger number of PN couples leads to a smaller difference of volumetric specific power between the ATEG and the FTEG. Besides, within a specific module length, $P_{\text{vsp-ATEG}}$ is always higher than $P_{\text{vsp-FTEG}}$. However, due to the very small size of the thermocouples, the power output of ATEG is slightly higher than FTEG in the entire TEM system. This exhibits that the ATEG has a superior thermoelectric conversion performance with the same PN couples volume.

The change of P_{vsp} with the volume of thermoelectric semiconductors at different inlet temperatures is shown in Fig. 10(b). Similar to the previous case, the volumetric specific power difference between ATEG and FTEG decreases as the volume of PN couples increases. The difference is that the exhaust gas inlet temperature has a greater impact on ΔP_{vsp}. It means that the higher the exhaust gas temperature is, the

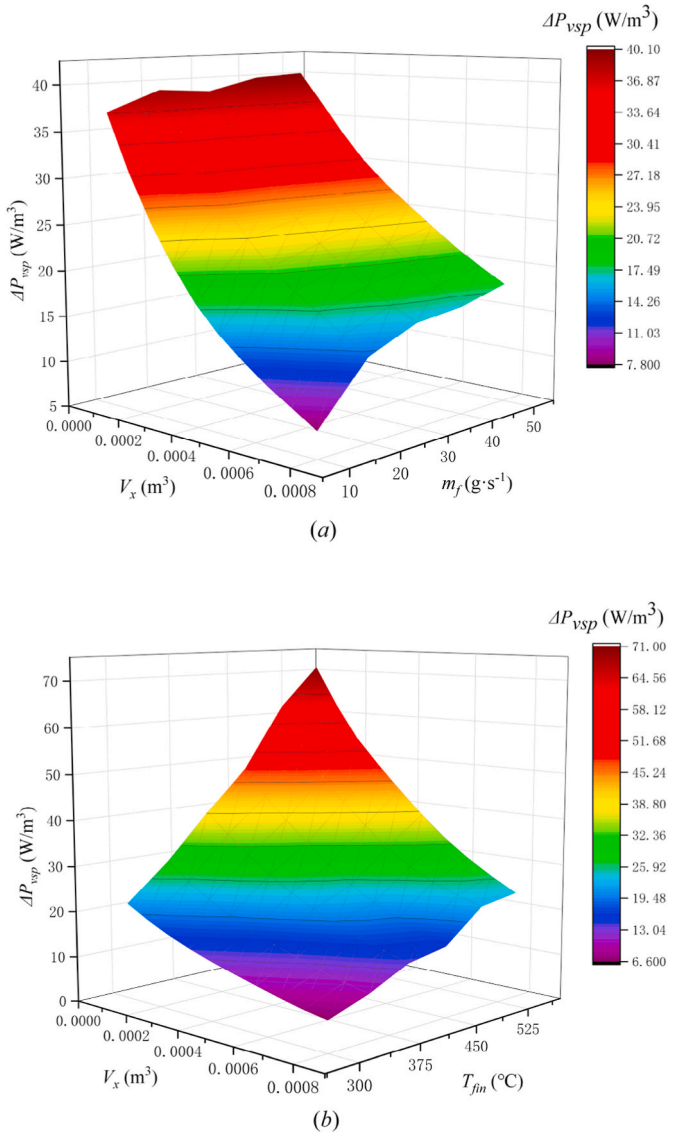

Fig. 10. ΔP_{vsp} versus the volume of PN couples at different (a) mass flow rates and (b) exhaust inlet temperatures.

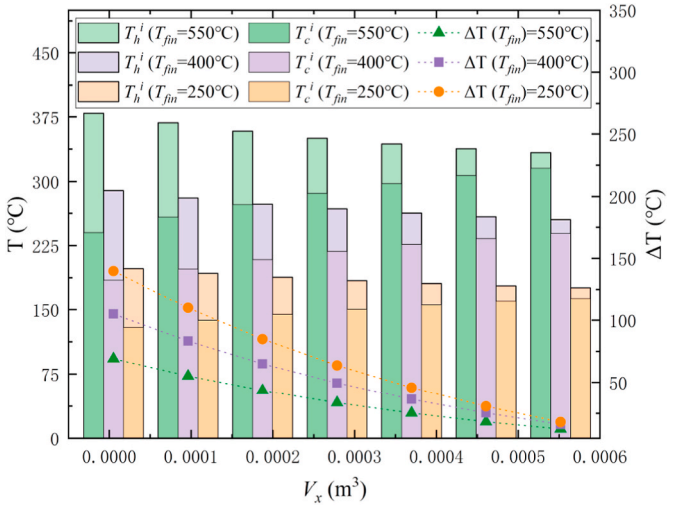

Fig. 11. ATEG temperature distributions with different T_{fin} (based on P_{ATEG}).

greater the ΔP_{vsp}.

The results in Fig. 10 show that the ATEG has a slightly higher electrical power output than the FTEG under the same PN couples volume. As confirmed by Mannikandan et al. [14], this is mainly due to the better heat transmission performance of ATEGs with a larger heat transfer area.

4.2. *Effects of different exhaust parameters on the thermoelectric performance of ATEGs*

Since the exhaust gas temperature of an automobile engine fluctuates between 250 °C and 600 °C, mass flow rate fluctuates between 10 g s^{-1} and 50 g s^{-1} for a long time after operation [27], the effects of different exhaust temperatures and mass flow rates on the ATEG thermoelectric performance are analyzed in Section 4.2.1 and Section 4.2.2, respectively.

4.2.1. *Influence of fluctuating gas temperature*

Aiming at maximizing the ATEG output power, the temperature distribution of the cold end and the hot end of the module is shown in Fig. 11. The thermoelectric semiconductor volume is optimally designed at the above three temperatures and the temperature difference

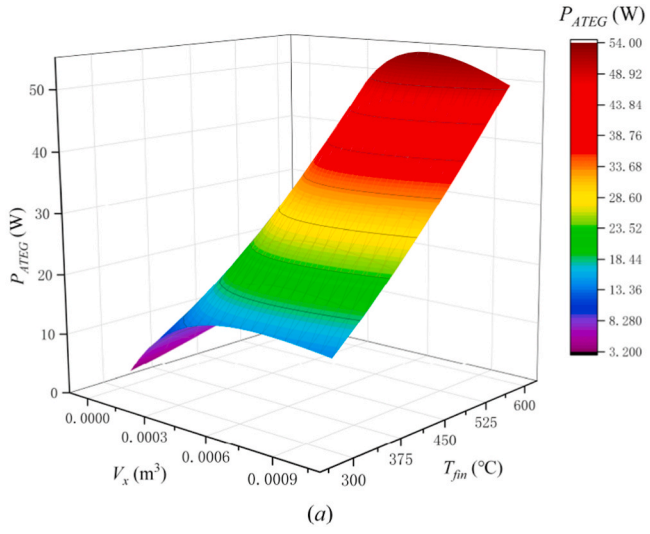

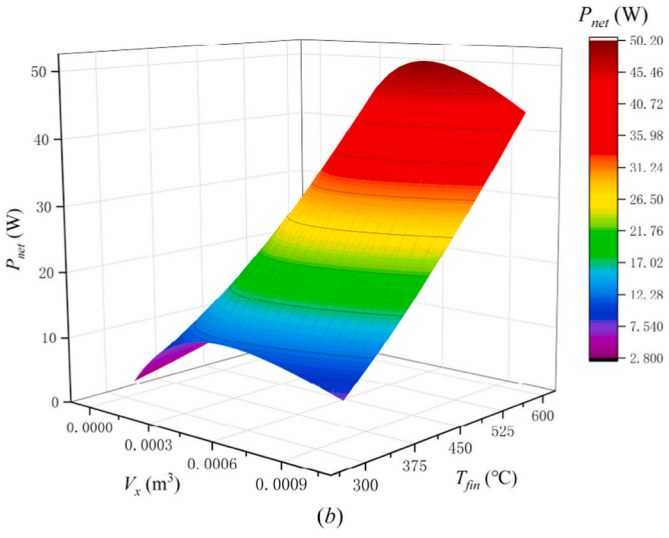

Fig. 12. (a) Output power and(b) net power versus PN couples volume with different T_{fin}.

distributions. At different inlet temperatures, the trend of temperature difference on both ends of thermocouples is almost the same, whereas the optimal semiconductor volume has shown some difference. Furthermore, it can be seen that at the same thermocouple length, a higher exhaust gas temperature always leads to a more significant temperature difference between the hot and the cold ends. Although the intake air temperature differs, the temperature difference at the exit of the ATEG is very similar. This is because of the strong convection heat transfer effect between the hot(cold) fluid and the thermocouple. Most of the thermal energy of the hot side is transmitted to the cold side.

Fig. 12(a) shows the variation in power output of the ATEG with the total PN couples volume under different exhaust temperatures. The exhaust gas inlet temperature has little effect on the optimal semiconductor volume of the ATEG, which is consistent with the analysis in Fig. 11. Meanwhile, the maximum output power of ATEG is approximately linearly increasing with the exhaust gas temperature. In this case, the optimal PN couples volume of the module is about $V_{opt} = 6.58 \times 10^{-4}$ m^3, the corresponding n_x is 130.

Fig. 12(b) shows the variation of the net power with PN couples volume at different gas temperatures. The higher the hot fluid inlet temperature, the greater the corresponding optimal module semiconductor volume. In this case, the optimal PN couples volume of the module is between 5.06×10^{-4} m^3 and 6.07×10^{-4} m^3, the corresponding n_x is 100–120.

4.2.2. Influence of mass flow rates

When the exhaust gas parameter m_f fluctuates between 10 g s^{-1} and 50 g s^{-1}, the effects on the power output and the net power of the ATEG are analyzed as follows. Fig. 13 shows the optimal temperature difference and distribution of the two ends of thermocouples at different m_f when the maximum output power is obtained. The temperature variation of ATEG shows a significant difference under different mass flow rates. The mass flow rate is positively correlated with the optimal semiconductor volume, and the larger mass flow will result in a larger optimal semiconductor volume. When the mass flow is higher than 30 g s^{-1}, both the temperatures of the two ends of thermocouples increase continuously with the increase of semiconductor volume. From Fig. 13, the parameters of cooling fluid and thermal resistance of the ATEM remain unchanged when $m_f = 50$ g s^{-1}. However, the thermal energy of the exhaust gas cannot be absorbed entirely, leading to an increase in the average temperature of the entire ATEG. Because of the convection heat transfer of the hot and cold fluid, the mass flow rate of exhaust has little effect on the temperature difference at the exit of the ATEG.

The changes in power output (P_{ATEG}) with PN couples volume at different mass flow rates are shown in Fig. 14(a). When $m_f < 30$ g s^{-1}, the optimal PN couples volume increases obviously with the increase of m_f, which shows that m_f has a great influence on the selection of PN couples volume. However, the optimal PN couples volume increases more slowly at high mass flow rates. The optimal PN couples volume of the module ranges from 3.54×10^{-4} m^3 to 7.59×10^{-4} m^3, the corresponding n_x is 70–150.

Fig. 14(b) shows the changes in net power (P_{net}) with PN couples volume at different flow rates. Both the maximum net power and the corresponding optimal PN volume V_{opt} increase with the increase of m_f when $m_f < 30$ g s^{-1}. However, when m_f is above a certain threshold, the peak net power of ATEG begins to decline rapidly. This can cause a negative net power when m_f exceeds 50 g s^{-1}. The main reason for this phenomenon is that a high pumping-power loss is produced at a high exhaust mass flow rate, resulting in a rapid decrease in net power as the length of the module increases. In this case, the optimal PN couples volume of the module is between 1.51×10^{-4} m^3 and 5.56×10^{-4} m^3, the corresponding n_x is 30–110.

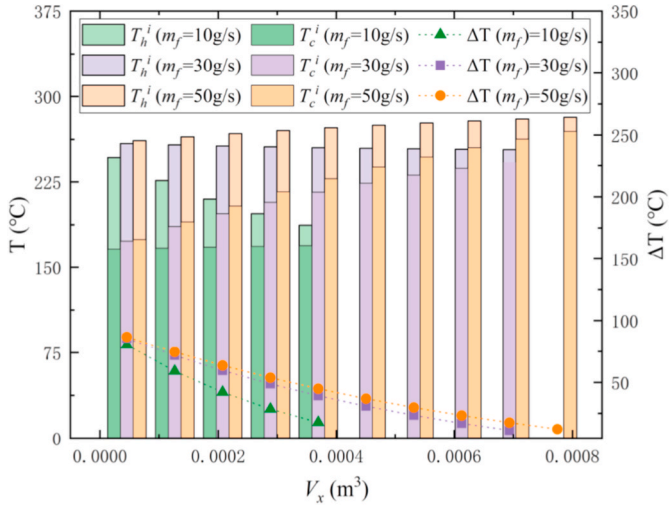

Fig. 13. Temperature gradient distribution under the optimal module length at different m_f.

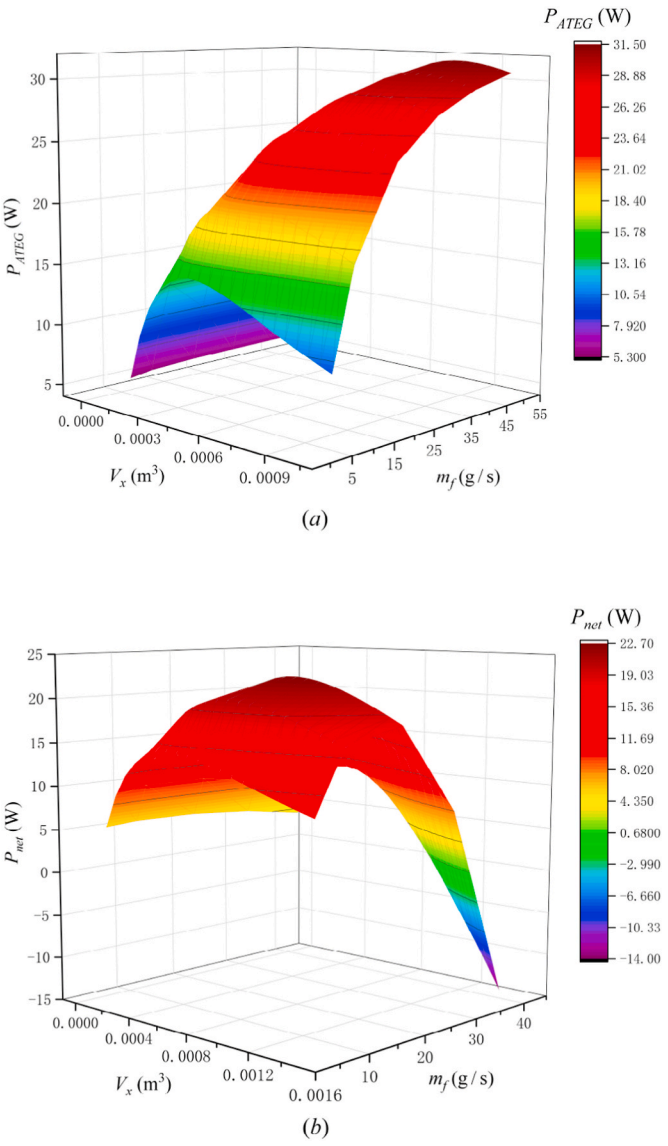

Fig. 14. (a) Output power and (b) Net power versus PN couples volume at different m_f.

4.3. Optimal design considering system economy

Based on the analysis in the previous section, the influence of different vehicle exhaust parameters on ATEG thermoelectric conversion characteristics and the optimal PN volume under different working conditions are obtained. However, in the process of automobile driving, the exhaust parameters fluctuate for a longer time in some ranges, which should be considered in the design of the ATEG system. In this subsection, combining the application of ATEG in automobiles and considering the fluctuation of automobile exhaust parameters, two optimization methods are proposed and compared to maximize the economic efficiency of the ATEG.

4.3.1. Weighted power deviation analysis

NEDC is a standard testing procedure to test the performance of vehicles in two scenarios corresponding to the urban area and suburban areas. The results can reflect the running state of the vehicle to a certain extent, and based on this dynamic condition, an optimal ATEG module volume can be designed. According to the proportion of different exhaust gas parameters in a cycle (C_T and C_m), the weighted power deviation coefficient is obtained by weighting the power deviation. In an NEDC driving cycle, the exhaust gas characteristic parameters produced by the BMW 530i equipped with an in-line 6-cylinder 3.0L gasoline engine are shown in Table 3 [32].

According to the previous analysis, the optimal PN volume V_x is supposed to be within $[V_{\min},V_{\max}]$ to obtain high net power. The power deviation between P_{net} obtained at different PN couples volumes and the peak net power $P_{\text{net,max}}$ obtained at the optimal volume is

$$dev = \left(P_{\text{net,max}} - P_{\text{net}}\right)/P_{\text{net,max}} \tag{20}$$

The weight of exhaust gas m_f is assigned to the power deviation, which is denoted as dev_m, and the weight of temperature T_{fin} is assigned to the sum value of dev_m at different mass flows, denoted as $dev_{m,T}$. In this study, the exhaust gas of 250–350 °C is classified as 300 °C, and so on. Furthermore, when the volume of PN couples is selected within $[V_{\min},V_{\max}]$, different $dev_{m,T}$ values will be obtained. The optimal design volume of PN couples with the maximum net power under the condition of fluctuation of exhaust parameters should be selected by minimizing $dev_{m,T}$. Thus, the objective function is constructed by minimizing the sum of $dev_{m,T}$ at different temperatures. The designed volume of PN couples is taken as the independent variable. The optimization objective and the constraints are

$$\begin{aligned} \min \quad & \sum_{Tfin=300\ ^\circ\text{C}}^{Tfin=600\ ^\circ\text{C}} dev_{m,T} \\ \text{s.t.} \quad & \begin{cases} dev_m = \left[\left(P_{\text{net,max}} - P_{\text{net}}\right)/P_{\text{net,max}}\right] \times C_m \\ dev_{m,T} = C_T \times \sum_{mf=5\ \text{g s}^{-1}}^{mf=50\ \text{g s}^{-1}} dev_m \\ V_x \in [V_{\min}, V_{\max}] \\ m_f \in \left[5\ \ \text{g}\cdot\text{s}^{-1}, 50\ \ \text{g}\cdot\text{s}^{-1}\right] \\ T_{fin} \in [300\ \ ^\circ\text{C}, 600\ ^\circ\text{C}] \end{cases} \end{aligned} \tag{21}$$

Table 3
Exhaust gas parameter weight.

Temperature	C_T	Mass flow rate	C_m
<250 °C	10.5%	<5 g s^{-1}	9.1%
250–350°C	48.6%	5–15 g s^{-1}	66.8%
350–450°C	31.5%	15–25 g s^{-1}	14.8%
450–550°C	7.2%	25–35 g s^{-1}	7.4%
550–650°C	2.2%	35–45 g s^{-1}	1.6%
>650°C	0	>45 g s^{-1}	0.3%

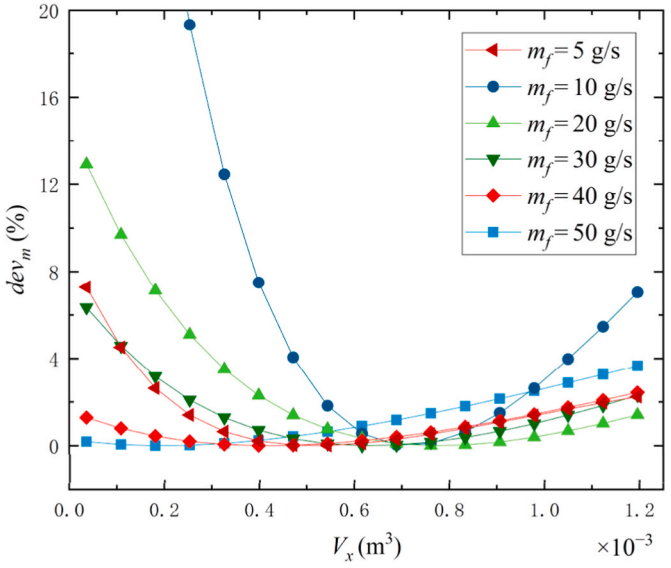

Fig. 15. Weighted power deviation versus PN couples volume for different m_f.

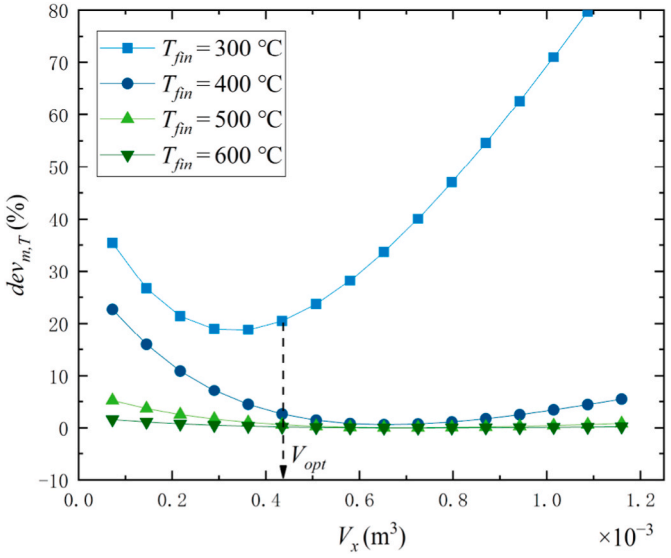

Fig. 16. Relationship between weighted power deviation and PN couples volume for different T_{fin}.

Fig. 15 shows the weight power deviation dev_m under different m_f when the hot fluid temperature is fixed at 400 °C. The greater the weight of m_f, the greater the value of dev_m. The curve of $dev_{m,T}$ at 400 °C can be obtained by multiplying the sum of dev_m at different m_f in Fig. 18 by the temperature weight C_T.

Fig. 16 shows the changes in $dev_{m,T}$ with the designed PN couples volume at different gas temperatures when considering the fluctuation of mass flow rate. Automobile engine exhaust temperature shows an obvious influence on the weighted power deviation. The $dev_{m,T}$ value at different temperatures decreases first. It then increases, and the minimum weight power deviation is obtained at different volumes of PN couples. The minimum value of the sum of $dev_{m,T}$ at different temperatures is 23.91%, the optimal volume of PN couples is 4.35 × 10^{-4} m^3, and the corresponding n_x is 60.

4.3.2. Multi-objective optimization based on NSGA-II

The design method of ATEG based on weighted power deviation analysis in Section 4.3.1 can ensure to the greatest extent that the TEM

can obtain higher net power under various vehicle operating conditions. However, in addition to maximizing the net power to design a TEG, the energy conversion efficiency and the generator cost must also be considered. The net power reflects the power output capacity of TEGs, the thermoelectric conversion efficiency measures the ability to convert thermal energy into electrical energy, and the cost is a critical factor for practical applications. These three factors comprehensively reflect the economic performance of TEGs. Therefore, in order to obtain the optimal vehicle-mounted TEG configuration, in addition to the thermocouple configuration, vehicle exhaust back pressure, net power, and efficiency, the cost factor of the TEG system needs to be considered.

For an efficient ATEG system, higher net power output and lower total investment costs should be obtained. In the previous literature on the economic evaluation of thermoelectric systems, many different cost calculations have been established [33,34]. Based on the contributions of these articles, this paper extracts some research results. It combines the characteristics of the ATEG to establish the cost evaluation coefficient to estimate the cost more accurately [35–39].

The main costs of the vehicle-mounted ATEG include the cost of thermoelectric raw materials (G_m), the costs of other materials of ATEM (G_c) [35,36], manufacturing cost related to processing bulk materials (G_{ma}), modular cost (G_{mb}) [37,38], heat exchanger cost (G_{hex}), system balance cost (G_b), and installation cost (G_i) [39]. As the ring-shaped TEM is directly attached to the outside of the exhaust pipe in this study, the cost of the heat exchanger is not considered. One of the major benefits of the automotive ATEG system is that it has no moving parts. Therefore, the operation and maintenance costs are also neglected. The generation cost of the ATEG is thus expressed as follows.

$$G_{tot} = G_m + G_c + G_{ma} + G_{mb} + G_{hex} + G_b + G_i \tag{22}$$

$$G_m = G_m^* \cdot \rho \cdot V_x \tag{23}$$

$$G_c = G_c^* \cdot (S_h + S_c) \cdot n_x \cdot n_r \tag{24}$$

$$G_{ma} = G_{ma}^* \cdot \rho \cdot V_x \tag{25}$$

$$\begin{aligned} G_{mb} &= G_{mb}^* \cdot n_r \cdot n_x \cdot (S_h + S_c) / 2 \\ &= \left(G_D^* + G_M^* + G_{MLM}^* + G_{SP}^*\right) \cdot n_r \cdot n_x \cdot (S_h + S_c) / 2 \end{aligned} \tag{26}$$

$$G_b + G_i = 0.2 \cdot (G_m + G_c + G_{ma} + G_{mb}) \tag{27}$$

where $G^*\ m = 110$ \$/kg represents the average price of thermoelectric semiconductor materials, $\rho = 7740$ kg/m^3 represents the average density of the Bi_2Te_3 material, G* c = 1000 \$/m^2 represents the cost per unit area of other materials (including ceramic substrates, copper sheets, and wires, etc.) of the ATEM, and $G^*\ ma = 1.3$ \$/kg represents the cost per unit mass of thermoelectric material processed into ATEC using spark plasma sintering (SPS) technology. $G^*\ mb$ represents the manufacturing cost per unit area of the ATEM, using cutting, metallization, medium-level microfabrication, and silkscreen manufacturing processes. The specific cost includes cutting cost $G^*\ D$, 40 \$/m^2, metallization cost $G^*\ M$, 115 \$/m^2, medium level micro-manipulation processing cost $G^*\ MLM$, 2000 \$/m^2, silkscreen cost, 5 \$/m^2. Installation cost and system balance cost are considered as 10% of the ATEG manufacturing cost [36].

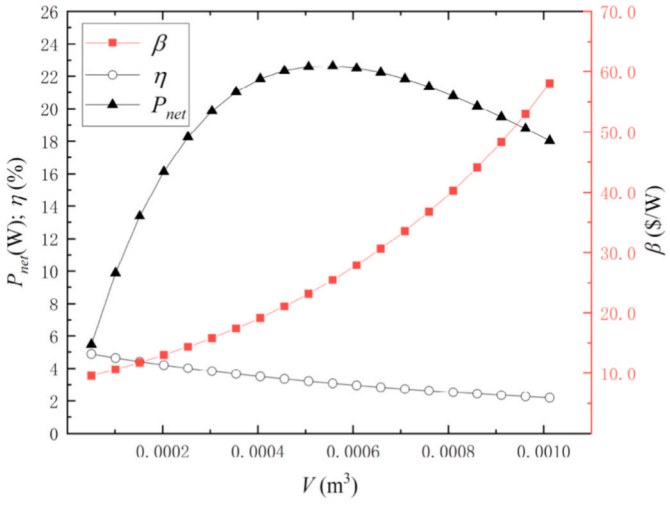

Fig. 17. Changes in the net power, efficiency and power generation cost with the total volume of the thermoelectric semiconductor.

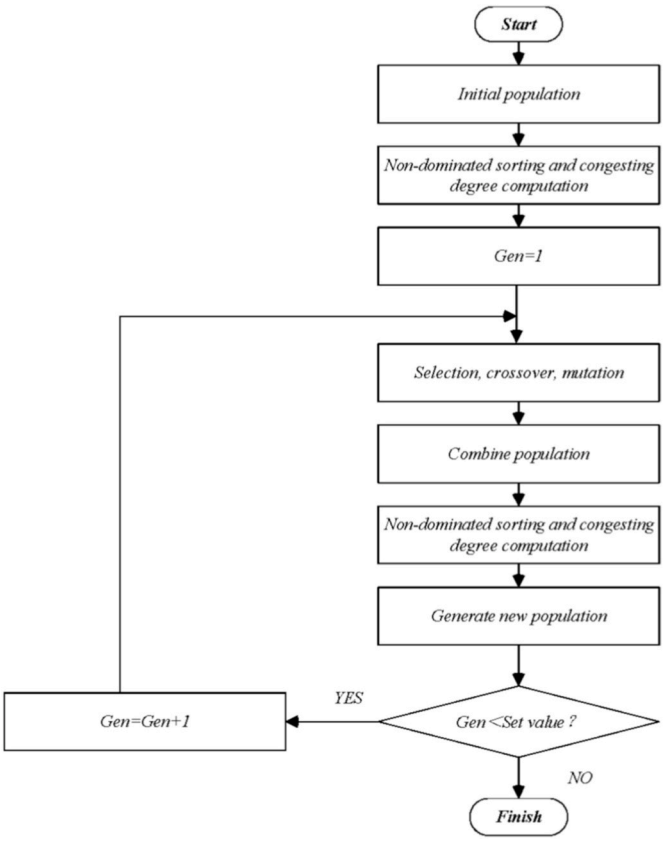

Fig. 18. Flow chart of NSGA-II.

Next, we define the cost per power β as the total cost index of the ATEG:

$$\beta = G_{\text{tot}} / P_{\text{net}} \tag{28}$$

The changes in the net power, efficiency, and power generation cost of ATEG with the total volume of the thermoelectric semiconductor are shown in Fig. 17. As the thermoelectric semiconductor volume increases, the net power first increases and then decreases, the efficiency decreases, and the power generation cost continues to increase. Therefore, to obtain the best economic performance of ATEG, high net power output, high energy conversion efficiency, and low power generation costs should be maintained. However, as shown in Fig. 17, these three performance indicators have conflicting relationships and cannot be optimized simultaneously.

Multi-objective evolutionary algorithm (MOEA) is a technique that minimizes/maximizes multiple objective functions under given boundary conditions and constraints. For this characteristic of ATEG, an MOEA can be used. Considering the total thermoelectric semiconductor volume and thermoelectric semiconductor volume in a single ring as the decision variables, the net power, efficiency, and power generation cost of the ATEG can be optimized simultaneously. The optimized result

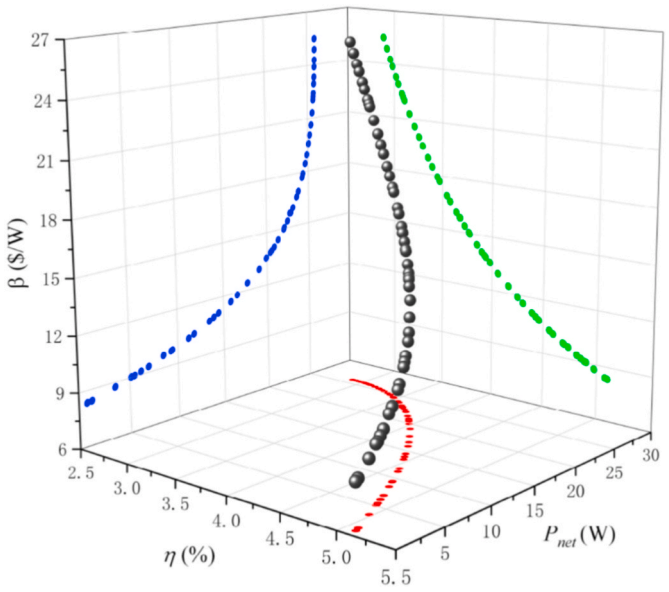

Fig. 19. Optimized results for net power, efficiency, and cost per power of ATEG.

represents an optimal set of compromises between multiple objective functions. By combining the ATEG model established in this work, the NSGA-II is used to optimize the three conflicting objective functions [40]. Fig. 18 shows the flow chart of the NSGA-II procedure. The algorithm parameters are set as follows: The population size is 300, the crossover probability is 1, the mutation probability is 0.5 (1/number of decision variables), the maximum number of iterations is 250, and the crossover and mutation distribution indices are 10 and 50, respectively.

According to the analysis of the TEG characteristics under different exhaust parameters in Section 4.4, taking this range as the boundary condition. Considering the contradiction between the output power, efficiency and power generation cost of ATEG, i.e., the optimal value cannot be obtained simultaneously. Therefore, this optimization problem is transformed into the following form.

$$\begin{aligned} &Max \;\; J_1 = f_1(V_{xd}, V_{rd}) \\ &Max \;\; J_2 = f_2(V_{xd}, V_{rd}) \\ &Min \;\; J_3 = f_3(V_{xd}, V_{rd}) \end{aligned} \tag{29}$$

The functions J_1, J_2, and J_3 are designed to maximize the net power and efficiency of the TEG while minimizing its power generation cost.

After the multi-objective optimization, a set of Pareto solution sets are obtained. Therefore, it is necessary to determine the best solution amongst the optimization results. TOPSIS is a practical and classic multi-index evaluation method called technique for order preference by similarity to the ideal solution [41]. It sorts the candidate plans by calculating how close each plan is to the best and worst. In the optimization process of this paper, the best solution is maximizing the net power and efficiency of ATEG and minimizing the power generation cost, while the worst is the opposite.

Fig. 19 shows a set of three-dimensional Pareto frontier obtained after running NSGA-II. All solutions are non-dominated solutions. The

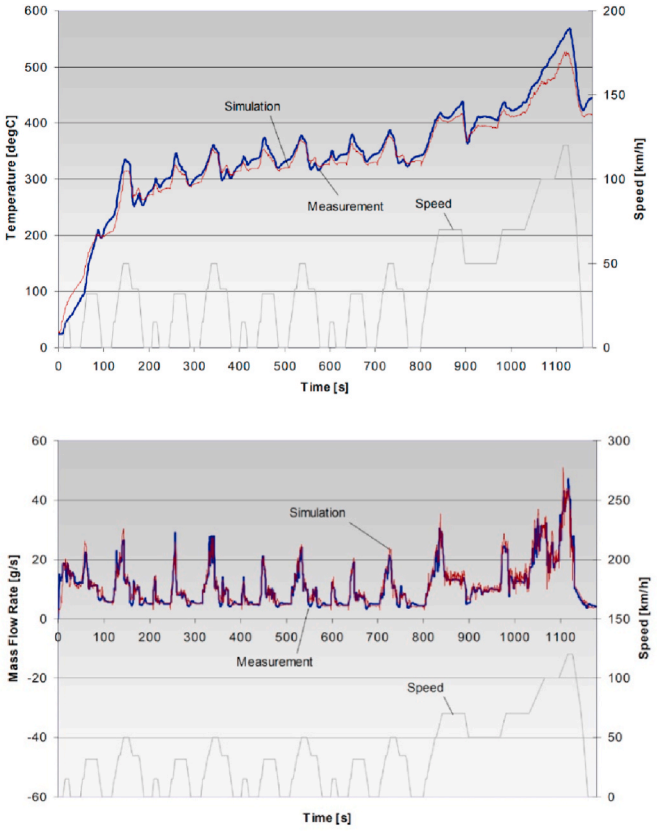

Fig. 20. Parameters profile of the exhaust gas in an NEDC [27].

greater the power of ATEG, the more thermoelectric semiconductor volume and the longer TEG length are required. As a result, the temperature difference between the two ends of the thermocouple changes greatly, leading to an increase in thermal energy loss and exhaust back pressure. Therefore, the conversion efficiency is reduced, and the cost of power generation will also increase.

The comparison of the optimal schemes selected by TOPSIS and the weighted power deviation analysis method proposed in Section 4.5 is shown in Table 4. Fig. 20 shows the changes of BMW 530i exhaust parameters with vehicle speed in an NEDC [27]. According to the changes of this parameter, the generated electrical energy of the two optimal schemes in an NEDC is calculated and provided in Table 4. In the optimal scheme selected by TOPSIS, the net power, efficiency, and power generation cost are better than the optimal solution determined by weighted power deviation analysis, but the generated electrical energy in an NEDC cycle is reversed. It shows that NSGA-II successfully optimized the configuration of the thermoelectric semiconductor volume in the ATEG under fixed working conditions and obtained the optimal ATEG performance. Meanwhile, it shows that when the exhaust gas parameters change with the operating conditions of the vehicle, higher electrical energy can be obtained with the optimal scheme determined by the weighted power deviation analysis method. When considering the power generation cost factor, the power generation cost of the optimal

Table 4
Comparison of optimal solution selected by TOPSIS and weighted power deviation method.

The optimal solution	Design variables		Performances			Amount of electricity generated within a NEDC cycle (W·h)	Total cost ($)
	Semiconductor volume in a single ring (m^3)	Total semiconductor volume (m^3)	P_{net} (W)	η (%)	β ($/W)		
TOPSIS	5.0625×10^{-6}	2.835×10^{-4}	20.85	3.9	14.08	4.35	293.08
Weighted power deviation	5.0625×10^{-6}	4.35×10^{-4}	19.86	3.82	15.81	5.7	450.9

solution determined by the weighted power deviation is 54% higher than the cost of the optimal scheme determined by the TOPSIS decision after NSGA-II optimization, but the generated electrical energy in an NEDC is only 31% higher. Therefore, considering the net power, efficiency, cost per power, generated electrical energy, and total cost of the ATEG, the optimal thermoelectric semiconductor volume configuration determined by the NSGA-II and the TOPSIS is obtained. The result shows that the optimal thermoelectric semiconductor volume of a single ring is 5.0625×10^{-6} m^3 and the total thermoelectric semiconductor volume is 2.835×10^{-4} m^3.

However, limited by the thermoelectric conversion capability of current commercial thermoelectric materials, their efficiency and power generation are still low, and the wide commercial application of annular thermoelectric generators in automobiles still needs extensive studies. With the continuous optimization of the structure and ZT value of thermoelectric semiconductor materials, the power generation of ATEGs will be significantly improved in the future.

5. Conclusions

When using annular thermoelectric generators (ATEGs) to recover thermal energy from unstable heat sources such as automobile waste exhaust, it is essential to consider the non-trivial parameters change to optimize the thermoelectric performance. The influence of different exhaust parameters on the thermoelectric performance of ATEG was studied, and the configuration of the ATEG system was optimized through the weighted power deviation method and NSGA-II. The main conclusions obtained in this study are as follows.

1) Within a certain range of exhaust parameters, the volumetric specific power of ATEG is higher than that of FTEG, while the electrical power output of ATEG is slightly higher under the same volume of PN couples. The difference between the volumetric specific power of ATEG and FTEG decreases as the volume of PN couples increases.
2) As the volume of PN couples increases, both the net power and the output power of the system increase first and then decrease. When aiming to maximize the net power of ATEG, the optimal thermoelectric semiconductor volume is more influenced by mass flow rates than the engine exhaust gas temperature. The optimal design range of annular thermoelectric semiconductor volume is 1.51×10^{-4} m^3 – 7.59×10^{-4} m^3.
3) Using the weighted power deviation analysis method proposed in this paper, the optimal PN couples volume is 4.35×10^{-4} m^3. The vehicle can obtain a high net output power under various working conditions.
4) The Pareto solution set and the optimal design point are obtained based on multi-objective optimization. The PN couple volume in a single ring is 5.0625×10^{-6} m^3 and the total PN couple volume is 2.835×10^{-4}. It is shown that the NSGA-II is superior to the weighted power deviation method in terms of the optimization result under the NEDC test driving profile. The optimal output power is 20.85 W, the efficiency is 3.9%, and the cost per power is 14.08.

In addition to improving the thermoelectric semiconductor configuration, there is a potential to further enhance the performance of the ATEGs. For example, one can improve the heat transfer, increase heat transfer area, and control the increase in exhaust pressure drop. Related studies are ongoing, and results will be presented in future works.

CRediT authorship contribution statement

WenChao Zhu: Data curation, Funding acquisition, Investigation, Methodology. **Wenlong Yang:** Data curation, Writing – original draft. **Yang Yang:** Conceptualization, Software, Validation. **Yang Li:** Formal analysis, Investigation, Writing – review & editing. **Hao Li:** Formal analysis, Supervision. **Ying Shi:** Project administration. **Yonggao Yan:** Funding acquisition, Methodology, Validation. **Changjun Xie:** Conceptualization, Funding acquisition, Project administration, Supervision, Writing – review & editing.

Declaration of competing interest

The authors declare that they have no known competing financial interests or personal relationships that could have appeared to influence the work reported in this paper.

Acknowledgments

This research was supported by the National Natural Science Foundation of China (51977164), and the Wuhan Frontier Project on Applied Research Foundation (2019010701011405). This research was also supported by China Scholarship Council(202106950031)。

References

[1] C. Amaral, C. Brandão, É.V. Sempels, F.J. Lesage, Net thermoelectric generator power output using inner channel geometries with alternating flow impeding panels, Appl. Therm. Eng. 65 (2014) 94–101.
[2] Y. Ge, K. He, L. Xiao, W. Yuan, S.-M. Huang, Geometric optimization for the thermoelectric generator with variable cross-section legs by coupling finite element method and optimization algorithm, Renew. Energy 183 (2022) 294–303.
[3] X. Li, C. Xie, S. Quan, L. Huang, W. Fang, Energy management strategy of thermoelectric generation for localized air conditioners in commercial vehicles based on 48 V electrical system, Appl. Energy 231 (2018) 887–900.
[4] Y. Li, B. Xiong, D.M. Vilathgamuwa, Z. Wei, C. Xie, C. Zou, Constrained ensemble Kalman filter for distributed electrochemical state estimation of lithium-ion batteries, IEEE Trans. Ind. Inf. 17 (1) (2021) 240–250.
[5] X. Li, C. Xie, S. Quan, Y. Shi, Z. Tang, Optimization of thermoelectric modules' number and distribution pattern in an automotive exhaust thermoelectric generator, IEEE Access 7 (2019) 72143–72157.
[6] E. Massaguer, A. Massaguer, T. Pujol, M. Comamala, L. Montoro, J.R. Gonzalez, Fuel economy analysis under a WLTP cycle on a mid-size vehicle equipped with a thermoelectric energy recovery system, Energy 179 (2019) 306–314.
[7] D. Luo, R. Wang, W. Yu, W. Zhou, Parametric study of a thermoelectric module used for both power generation and cooling, Renew. Energy 154 (2020) 542–552.
[8] X. Liu, Y. Deng, Z. Li, C. Su, Performance analysis of a waste heat recovery thermoelectric generation system for automotive application, Energy Convers. Manag. 90 (2015) 121–127.
[9] G. Shu, X. Ma, H. Tian, H. Yang, T. Chen, X. Li, Configuration optimization of the segmented modules in an exhaust-based thermoelectric generator for engine waste heat recovery, Energy 160 (2018) 612–624.
[10] H.-B. Liu, S.-L. Wang, Y.-R. Yang, W.-H. Chen, X.-D. Wang, Theoretical analysis of performance of variable cross-section thermoelectric generators: effects of shape factor and thermal boundary conditions, Energy 201 (2020), 117660.
[11] E. Bellos, C. Tzivanidis, Energy and financial analysis of a solar driven thermoelectric generator, J. Clean. Prod. 264 (2020), 121534.
[12] Y. Choi, A. Negash, T.Y. Kim, Waste heat recovery of diesel engine using porous medium-assisted thermoelectric generator equipped with customized thermo electric modules, Energy Convers. Manag. 197 (2019), 111902.
[13] Z.G. Shen, S.-Y. Wu, L. Xiao, Theoretical analysis on the performance of annular thermoelectric couple, Energy Convers. Manag. 89 (2015) 244–250.
[14] S.C. Kaushik, S. Manikandan, The influence of Thomson effect in the energy and exergy efficiency of an annular thermoelectric generator, Energy Convers. Manag. 103 (2015) 200–207.
[15] S. Manikandan, S.C. Kaushik, Energy and exergy analysis of solar heat pipe based annular thermoelectric generator system, Sol. Energy 135 (2016) 569–577.
[16] Z.-G. Shen, S. Wu, L. Xiao, Assessment of the performance of annular thermoelectric couples under constant heat flux condition, Energy Convers. Manag. 150 (2017) 704–713.
[17] W. Zhu, Z. Weng, Y. Li, L. Zhang, B. Zhao, C. Xie, Y. Shi, L. Huang, Y. Yan, Theoretical analysis of shape factor on performance of annular thermoelectric generators under different thermal boundary conditions, Energy 239 (2022), 122285.
[18] Z. Weng, F. Liu, W. Zhu, Y. Li, C. Xie, J. Deng, L. Huang, Performance improvement of variable-angle annular thermoelectric generators considering different boundary conditions, Appl. Energy 306 (2022), 118005.
[19] D. Luo, R. Wang, Y. Yan, Z. Sun, W. Zhou, R. Ding, Comparison of different fluid-thermal-electric multiphysics modeling approaches for thermoelectric generator systems, Renew. Energy 180 (2021) 1266–1277.
[20] W. He, S. Wang, X. Zhang, Y. Li, C. Lu, Optimization design method of thermoelectric generator based on exhaust gas parameters for recovery of engine waste heat, Energy 91 (2015) 1–9.
[21] A.E. Risseh, H. Nee, C. Goupil, Electrical power conditioning system for thermoelectric waste heat recovery in commercial vehicles, IEEE Trans. Transport. Electrific. 4 (2018) 548–562.

[22] D. Luo, R. Wang, W. Yu, W. Zhou, Performance optimization of a converging thermoelectric generator system via multiphysics simulations, Energy 204 (2020), 117974.
[23] W. Yang, W. Zhu, Y. Li, L. Zhang, B. Zhao, C. Xie, Y. Yan, L. Huang, Annular thermoelectric generator performance optimization analysis based on concentric annular heat exchanger, Energy 239 (2022), 122127.
[24] D. Luo, Y. Yan, R. Wang, W. Zhou, Numerical investigation on the dynamic response characteristics of a thermoelectric generator module under transient temperature excitations, Renew. Energy 170 (2021) 811–823.
[25] D. Luo, Z. Sun, R. Wang, Performance investigation of a thermoelectric generator system applied in automobile exhaust waste heat recovery, Energy 238 (2022), 121816.
[26] S. Mavridou, G.C. Mavropoulos, D. Bouris, D.T. Hountalas, G. Bergerles, Comparative design study of a diesel exhaust gas heat exchanger for truck applications with converntinal and stage of the art heat transfer enhancements, Appl. Therm. Eng. 30 (2010) 935–947.
[27] J. Lagrandeur, D. Crane, S. Hung, Automotive waste heat conversion to electric power using skutterudite, TAGS, PbTe and BiTe, thermoelectrics, in: 2006, ICT '06. 25th International Conference on IEEE, 2006.
[28] Y.J. Cui, B.L. Wang, K.F. Wang, L. Zheng, Power output evaluation of a porous annular thermoelectric generator for waste heat harvesting, Int. J. Heat Mass Tran. 137 (2019) 979–989.
[29] X. Niu, J. Yu, S. Wang, Experimental study on low-temperature waste heat thermoelectric generator, J. Power Sources 188 (2009) 621–626.
[30] H. Cui, Z. Shi, S. Yang, X. Yue, J. Meng, Engineering Fluid Mechanics, first ed., Petroleum industry press, Beijing, 1995.
[31] Y. Yang, S. Wang, Y. Zhu, Evaluation method for assessing heat transfer enhancement effect on performance improvement of thermoelectric generator systems, Appl. Energy 263 (2020), 114688.
[32] J. Pavlovic, A. Marotta, B. Ciuffo, CO_2 emissions and energy demands of vehicles tested under the NEDC and the new WLTP type approval test procedures, Appl. Energy 177 (2016) 661–670.
[33] H. Su, F. Zhou, H. Qi, J. Li, Design for thermoelectric power generation using subsurface coal fires, Energy 140 (2017) 929–940.
[34] H. Jaber, M. Ramadan, T. Lemenand, M. Khaled, Domestic thermoelectric cogeneration system optimization analysis, energy consumption and CO_2 emissions reduction, Appl. Therm. Eng. 130 (2018) 279–295.
[35] J.P. Bastos, G. Cunha, L.A. Barroso, T. Aquino, Reliability mechanism design: an economic approach to enhance adequate remuneration and enable efficient expansion, Energy 158 (2018) 1150–1159.
[36] M. Mirhosseini, A. Rezania, L. Rosendahl, Harvesting waste heat from cement kiln shell by thermoelectric system, Energy 168 (2019) 358–369.
[37] S.K. Yee, S. LeBlanc, K.E. Goodson, C. Dames, $ per W metrics for thermoelectric power generation: beyond ZT, Energy Environ. Sci. 6 (2013) 2561–2571.
[38] S. LeBlanc, S.K. Yee, M.L. Scullin, C. Dames, K.E. Goodson, Material and manufacturing cost considerations for thermoelectrics, Renew. Sustain. Energy Rev. 32 (2014) 313–327.
[39] A. Habibollahzade, E. Gholamian, P. Ahmadi, A. Behzadi, Multi-criteria optimization of an integrated energy system with thermoelectric generator, parabolic trough solar collector and electrolysis for hydrogen production, Int. J. Hydrogen Energy 43 (2018) 14140–14157.
[40] K. Deb, A. Pratap, S. Agarwal, T. Meyarivan, A fast and elitist multi-objective genetic algorithm: nsga-II, Evol. Comput. IEEE Trans. 6 (2002) 182–197.
[41] Y. Ge, Z. Liu, H. Sun, W. Liu, Optimal design of a segmented thermoelectric generator based on three-dimensional numerical simulation and multi-objective genetic algorithm, Energy 147 (2018) 1060–1069.